PCCP

PAPER

View Article Online
View Journal | View Issue

Cite this: *Phys. Chem. Chem. Phys.*, 2016, **18**, 28932

Remote joule heating assisted carrier transport in MWCNTs probed at nanosecond time scale†

Abhishek Mishra and Mayank Shrivastava*

Received 27th June 2016,
Accepted 16th September 2016

DOI: 10.1039/c6cp04497b

www.rsc.org/pccp

Quantum model of joule heating relies on electron–phonon scattering in the high field region (hot side contact), which locally increases phonon population and forms hot spots. Hot spots in the high field region are known to suffer carrier transport. In this work, for the first time we report remote joule heating of the cold side contact, *i.e.* zero electric field region, through multi-walled CNTs (MWCNTs), which is discovered to assist in carrier transport through the MWCNT channels. To precisely capture the dynamics of remote joule heating assisted carrier transport, MWCNTs are probed at nanosecond time scales. This leverages investigations at time scales comparable to characteristic thermal diffusion times and allows electron–phonon interactions and the nature of carrier transport to be probed under non-equilibrium conditions.

1 Introduction

Multi-walled carbon nanotubes (MWCNTs)[1] show extraordinary current carrying capacity under low-bias conditions.[2–4] However, when moderate or high electric fields are applied across CNTs, increased electron–phonon interaction leads to saturation in current. For example, the mean free path of a 500 nm long ballistic CNT falls to 40 nm at an applied bias of 2 V with optical phonon energy of 160 meV,[5,6] which shows that a moderate field across the channel is sufficient to populate it with optical phonons and hide some of the intricate features at higher fields. Optical phonons are high-energy, slow decaying vibrational modes, which contribute significantly towards hot spot formation. If the optical phonon population is not controlled, they can result in excessive channel heating,[7] which in turn can cause permanent damage to the device.[8–10] Moreover, higher phonon population and its coupling with electron transport affects the intrinsic nature of carrier transport, which hinders probing the intricate features related to electron–phonon transport at higher fields using conventional electrical methods. One of the ''intricate features'' addressed in this work is participation and contribution of high energy sub-bands[11,12] in carrier transport through the MWCNT channels as well as the metal–MWCNT contact.

Phonon population depends on electron–phonon interactions, which are intrinsic to the channel and cannot be controlled by merely controlling extrinsic parameters such as ambient temperature. Consequently, electron transport in MWCNTs and other 1D/2D channels at higher electric fields is not very clear and can only be usefully measured if the following two conditions are satisfied – (i) the electrical probe to study transport is applied for such a short duration that it does not lead to excessive self-heating and cause any damage to the device, and (ii) the corresponding response is sensed while the device is still in thermal non-equilibrium condition. Both the conditions together enable probing the intricate and hidden features of electrical transport at higher electric fields. Such a control can be achieved if the applied electrical probe is forced and sensed at the time scale comparable or smaller to the characteristic thermal diffusion time of the device. The characteristic thermal diffusion time of a 1D channel is the time taken by acoustic phonons to travel from the hot contact to the cold contact. The phonon population across the channel, and hence participation of sub-bands, keep rising during this time and saturates after a state of thermal equilibrium is reached. Hence, for example, participation of sub-bands and related aspects can be captured only if the channel is probed during the state of thermal non-equilibrium. The characteristic thermal diffusion time constant of MWCNTs is given by $L^2/(\pi^2\alpha)$, where L is the length of the tube and α is the thermal diffusivity.[13] The thermal diffusivity of MWCNTs is of the order of 10^{-5} m^2 s^{-1} as has been verified experimentally by using the 3-omega technique[14] and pulsed photo-thermal reflectance.[15] For a MWCNT with L = 1 μm the typical value of the thermal diffusion time is 5–30 ns. Consequently, in order to probe intricate features at higher electric fields, electron transport in MWCNTs should be probed at nanosecond time scales. It is worth highlighting that although a plethora of works exist which have presented the underlying physics of electron–phonon transport through MWCNTs,[16–20]

Advanced Nanoelectronic Device and Circuit Research Group, Department of Electronic Systems Engineering, Indian Institute of Science, Bangalore, 560012, India. E-mail: abhishekmishra@dese.iisc.ernet.in, mayank@dese.iisc.ernet.in; Tel: +91-80-2293-2732

† Electronic supplementary information (ESI) available. See DOI: 10.1039/c6cp04497b

none of them have captured the transport events keeping the above aspects in mind, and occurring at the time scale of a few nanoseconds. In this work, we delve deep into various mechanisms and events which are triggered simultaneously with the electrical probing of MWCNTs, at nanosecond time scales. This leverages investigations at time scales comparable to the characteristic thermal diffusion time and allows electron–phonon interactions and the nature of carrier transport to be probed under thermal non-equilibrium conditions. Although we have restricted our investigations to study the electron–phonon transport, the proposed method of nanosecond time scale investigation can be extended to study reaction kinetics in 1D and 2D materials under high field and high current conditions. For example, the time response of MWCNT breakdown can give an estimate of rate of oxidation of carbon under different conditions, which in turn can be used to derive the Arrhenius relation and extract the activation energy required for such a process. It is worth highlighting that an Arrhenius relation at nanosecond time scale is absent in the literature.

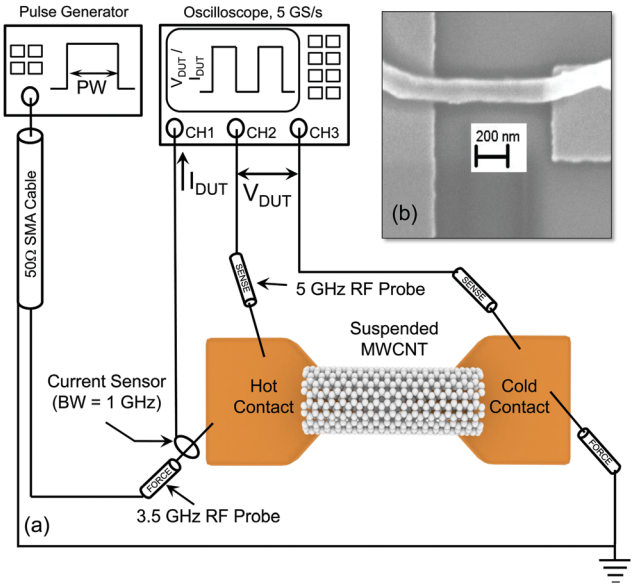

Fig. 1 (a) Nanosecond pulse *I*–*V* setup used in this work and (b) device under test (DUT).

2 Experimental

MWCNTs used in the experiments were grown using thermal CVD and deposited on metal electrodes (Cr/Pd 5 nm/50 nm on SiO_2) through dielectrophoresis[21] (10 MHz, 10 V_{P-P}) of a MWCNT suspension in DMF.[22] Post deposition, all tubes were observed under SEM. For nanosecond transport measurements only pairs of contacts bridged by single thick tube (50–100 nm in diameter) were selected. Devices with multiple tubes or thin tubes (diameter $<$ 50 nm) were discarded.

2.1 Contact pads for dielectrophoresis

1 cm $\times$ 1 cm SiO_2 (90 nm SiO_2 on P-doped Si) dies were cleaned using Piranha solution, followed by acetone, IPA wash and dehydration bake at 250 °C. Post cleaning, dies were spin coated with a stack of PMMA 495 A4 and PMMA 950 A2. For each layer of resist, spin coating was done at 6000 rpm for 2 min followed by 2 min of pre-bake at 180 °C. Thereafter, dielectrophoresis electrodes were patterned using e-beam lithography. Post exposure, patterns were developed using a solution of MIBK–IPA (1 : 3) for 25 s. For metallization, Cr/Pd (5 nm/50 nm) was evaporated in patterned electrodes. Lift-off was done in acetone, followed by IPA wash and dehydration bake. Palladium electrodes were used as they offer the least contact resistance with CNTs and graphene.

2.2 Aligned CNTs between contact pads

1 mg MWCNT powder was dispersed in 10 ml of *N*,*N*-dimethylformamide (DMF) through 30 min of bath sonication. DMF was preferred over other organic solvents due to its relatively lower vapour pressure, which resulted in decreased rate of evaporation and stable droplet formation during the process of dielectrophoresis. The suspension was then diluted serially by 100$\times$ and probe sonicated for 15 min at a mild power of 25 W and 20% pulsation. For dielectrophoresis, a 10 μl drop of the suspension was pipetted over the electrodes and AC signal of 10 V_{PP} and 10 MHz was applied on one side of a pair of electrodes, while the other side was kept floating. The AC signal was kept ON for 2 min, after which excess suspension was blown away. Post dielectrophoresis, dies were cleaned in warm DI water (90 °C), followed with acetone–IPA wash and dehydration bake (250 °C). The cleaning and annealing processes were done for 15 min each to ensure that the devices are free of contaminants and have minimum interface resistance.

2.3 Nanosecond pulse *I*–*V* setup

For electrical investigations, a nanosecond pulse *I*–*V* setup, as depicted in Fig. 1 was developed. After each pulse, current and voltage waveforms were captured using an oscilloscope with a sampling rate of 5 GS s^{-1}. Nanosecond scale voltage pulses were applied (forced) through a 50 Ω matched 3.5 GHz (G–S) RF probe, whereas the voltage across the DUT was measured (sensed) using a 5 GHz high impedance RF probe. A high bandwidth (1 GHz) current sensor with very high sensitivity was developed to probe sub-mA current at nanosecond time scale. Finally, by averaging the current and voltage waveform data over a fraction of pulse time (described in ESI†), single data point of the I_{DUT}–V_{DUT} characteristics was extracted.

3 Results and discussion

Fig. 2 shows the pulse *I*–*V* characteristics of a suspended MWCNT, characterized using nanosecond pulses with 20 and 80 ns pulse widths. One can clearly draw the following observations from Fig. 2 – (i) the current through the nanotube increases exponentially at pulse voltages above 3 V and (ii) the current and exponent increases as the pulse width is increased. Similar behavior was consistently noticed across a large set of nanotubes

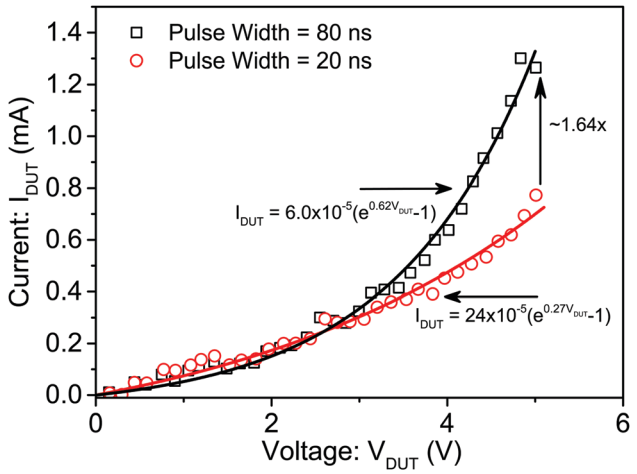

Fig. 2 Nanosecond pulse *I–V* characteristics of a suspended MWCNT, extracted using 20 and 80 ns long pulses.

characterized. These observations signify the presence of field and time dependent parameters which affect the carrier transport through the nanotubes. A similar sudden increase in current in the pre-breakdown region was reported previously,[23,24] but was not analyzed properly due to limitations of conventional measurement techniques. Fig. 3 shows the change in current through the nanotube as a function of time for different pulse voltages. The following observations can be drawn clearly: (i) the current rises linearly with time for a given pulse voltage and (ii) the rate of change in current with time *i.e.*, slope increases with increasing pulse voltage. Linear increase in current as a function of time indicates the presence of a time dependent parameter, which influences carrier transport through the nanotube and changes transport parameters as a function of time.

Current through a ballistic nanotube depends on the Fermi potential of contacts (electrical reservoirs), density of states and number of conduction channels (or modes) available for carrier

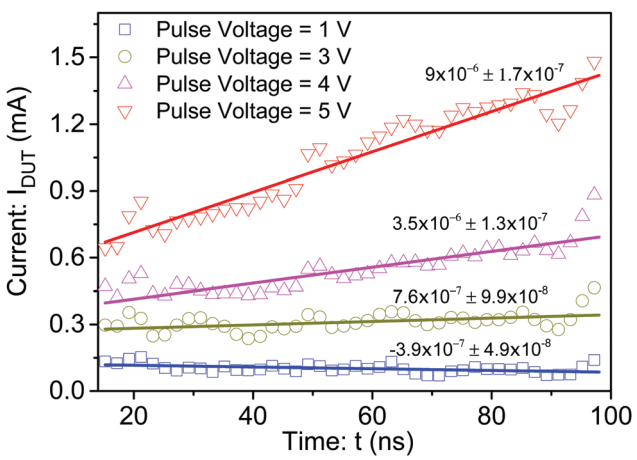

Fig. 3 Change in current through a suspended MWCNT with respect to time when the device was probed using nanosecond scale pulses. The rate at which the current increases rises with voltage pulse amplitude. Slope (A/ns^{-1}) is shown along with the curve.

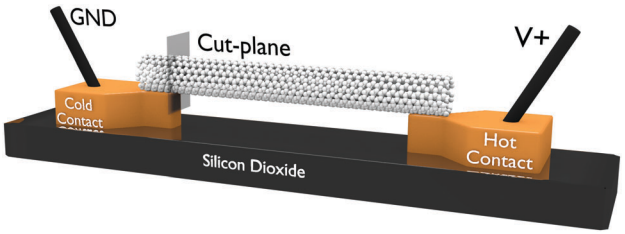

Fig. 4 Schematic view of MWCNT under test. Here hot and cold contacts represent electron reservoirs in which electrons, at the metal–CNT interface, have maximum and minimum energies, respectively. Cold contact/reservoir has relatively lower carrier energy and Fermi potential compared to hot contact.

transport.[25] For a given Fermi potential these quantities are time-independent; however, lattice heating with respect to time, due to electron–phonon scattering, can alter parameters defining carrier transport and therefore can result in change in current as a function of time. Fermi potential at the contacts, which is governed by the applied potential, should not change with temperature. Similarly, density of states depends on the crystal lattice, and can be safely considered to be independent of temperature assuming that the temperature is not high enough to change the lattice structure. Although the total number of conduction channels depends on the crystal structure and size, however, the number of conduction channels available for carrier transport strongly depends on the energy of carriers present inside the cold electrical reservoir (Fig. 4). Hence its dependence on the lattice temperature should be investigated.

In principle, electrons at room temperature, enter the channel from the electrically cold contact with carrier energy equivalent to thermal energy (kT/q), get accelerated and gain energy while traversing through the channel towards the hot contact, and finally undergo scattering with phonons in the electrically hot contact or electron reservoir. The metal electrodes (electron reservoirs) are also large phonon reservoirs and hence are assumed to be an ideal heat sink. However, since the nanotube and metal interact with weak van der Waals forces, which in turn results in high thermal interface resistance,[26] the electron–phonon scattering at the CNT–metal interface increases the phonon population, in spite of metal electrodes being large phonon reservoirs. The majority of phonons propagate towards the large phonon reservoir to attain lower energy states, however, a fraction of phonons propagate, through the CNT channel, towards the electrically cold phonon reservoir (Fig. 5). Flow of heat through MWCNT channel was experimentally investigated earlier by studying the change in state of sublimable material filled inside the tube.[27] The phonon transport follows the following relation:[28]

$$J_{\text{th}} = \sum_m \int_0^\infty \frac{dk}{2\pi} \hbar\omega_m(k) v_m(k) [\eta_{\text{hot}} - \eta_{\text{cold}}] T_m(k) \qquad (1)$$

where m is the mode index, $\omega_m(k)$ is the phonon dispersion relation for wave vector k, $v_m(k)$ is the group velocity, $T_m(k)$ is the transmission coefficient between mth mode and the reservoir and η gives the phonon population governed by Bose–Einstein statistics.

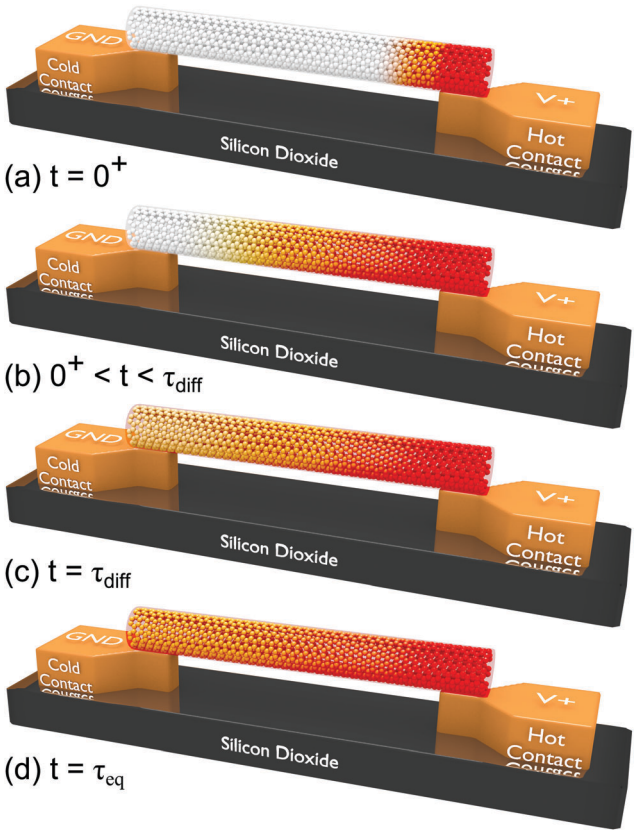

Fig. 5 Schematic view of temperature distribution across the MWCNT, probed at nanosecond time scale, depicted at different times. (a) $t = 0^+$: hot contact heats up due to thermalization of energetic electrons in metal–CNT interface; (b) $0 < t < \tau_{dif}$, heat energy flow/phonon transport towards the cold contact; (c) $t = \tau_{dif}$, remote joule heating of the cold contact, specifically the metal–CNT junction at the cold contact; (d) $t = \tau_{eq}$, device attains thermal equilibrium.

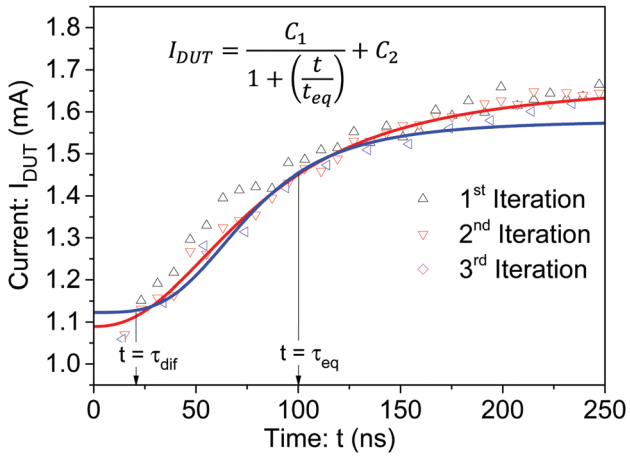

Fig. 6 Change in current through a suspended MWCNT with respect to time when device was probed using longer pulses to study the response before and after achieving thermal equilibrium. Pulse amplitude used here was 2.5 V. The behavior was found to be independent of the number of times the device was pumped with nanosecond pulses.

Fig. 6 shows the current as a function of time through MWCNT in response to a 250 ns long pulse applied in a repetitive fashion. The following interesting observations can be drawn from these measurements: (i) the trends are consistent and repetitive, hence the linear increase in current observed is independent of possible physical change in MWCNT or metal–MWCNT interface and is not attributable to current annealing. In addition to this, it shows that the current remains almost unchanged up to $t \sim 20$ ns, then increases linearly from 20 ns $< t <$ ~125 ns and saturates to a fixed current at $t > 125$ ns.

This behavior is explained in Fig. 5. For $0 < t < \tau_{dif}$, where τ_{dif} is the thermal diffusion time for the MWCNT under test, the cold electrode does not see any change in phonon population. Therefore up to $t = \tau_{dif}$ the current through the MWCNT remains unchanged. As the phonon population at the cold electrode increases at $t > \tau_{dif}$ (Fig. 5c), attributed to remote heating of the cold electrode, the current increases linearly as depicted above and explained in detail in the next paragraph. This continues until $t \sim t_{eq}$, where t_{eq} is the time taken to achieve thermal equilibrium (Fig. 5d). As the cold electrode does not see any further change in phonon population after achieving thermal equilibrium ($t > t_{eq}$), the current through the MWCNT does not increases further and saturates to a fixed value.

The question arises is why current increases linearly with time? Depending on the chirality, the individual shells of a MWCNT can either be metallic or semiconducting. Both of these shells have a series of non-crossing sub-bands. In addition, metallic tubes also have crossing sub-bands, and low bias conduction primarily happens through these bands.[29] Electrons in the cold side electrical reservoir with an energy distribution as defined by the local Fermi distribution, aligned with energy of these sub-bands, are transported through the MWCNT channel. However, the electrons with energies outside the sub-band energies are reflected back and do not participate in conduction. The local Fermi distribution, for example, here the Fermi distribution of electrons at the metal–MWCNT interface at the cold side electron reservoir, depends on the local lattice temperature/phonon population. In the absence of extrinsic heating, the joule heating at the hot electrode, which causes phonons to propagate towards the cold electrode and increase phonon population at the cold electrode, alters the Fermi distribution at the cold electrode–MWCNT interface. Such a remote joule heating spreads the Fermi distribution towards higher energies and populates higher energy sub-bands in accordance with the Fermi–Dirac distribution and increases the number of conducting channels (M). At temperature T, a CNT shell with diameter D and chirality $(n,0)$, contributes to M number of conducting channels, where M is given by:[30]

$$M(D,T) = \sum_{2n} \frac{1}{1 + e^{|E_v|/k_B T}} \quad (2)$$

Here, $E_v = \frac{3ta}{D}\left|v - \frac{2n}{3}\right|$, is the maximum energy of the v_{th} sub-band of a zigzag nanotube, t is the nearest neighbor hopping parameter and a is the interatomic distance. The above expression results in a linear rise in number of conduction channels with temperature as depicted in Fig. 7. It is well known from the

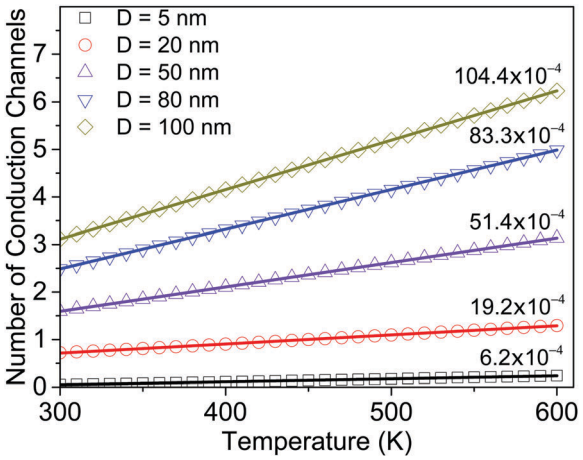

Fig. 7 Change in number of conduction channels with temperature, calculated for CNT shells with different tube diameters. The number of conduction channels increases linearly with temperature. Slope is shown along with the curve.

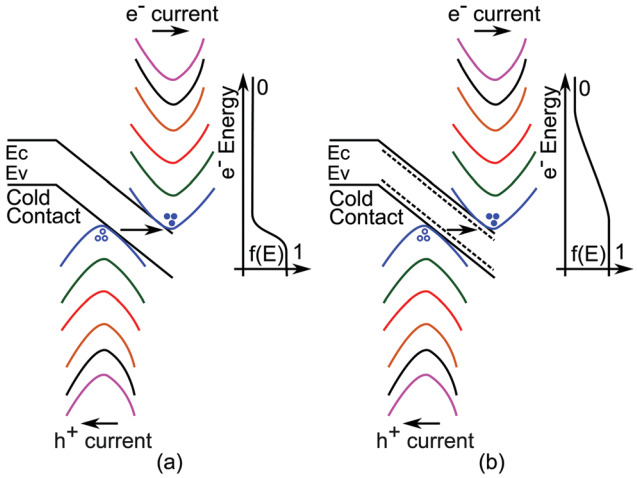

Fig. 8 Energy band diagrams of the shells at two different time instants along the cut-plane shown in Fig. 4; (a) $0^+ < t < \tau_{dif}$ and (b) $t > \tau_{dif}$.

solution of the time-dependent 1D Fourier equation for heat transport[31] that the temperature/phonon population at the cold electrode–CNT interface increases with time. Therefore, the number of conduction modes and hence current through the MWCNT increases with time. However, as soon as the device attains thermal equilibrium, the number of conduction channels does not change further and hence the current saturates at a fixed value. Note that the electrical conduction only due to electrons is considered, whereas the hole conduction is neglected. This assumption is based on the fact that band gap of a shell in CNT is given by $0.8/d$ eV, where d is diameter in nano-meters. Therefore, in a 50 nm thick MWCNT, the band gap diminishes and conduction happens primarily through electrons. Owing to the energy of these electrons, electron–phonon scattering, which results in contact heating should be considered only at the hot electrode. At a lattice temperature of T (which is room temperature in this work), electrons with energy kT/q enter the channel from the cold electrode and collide at the hot electrode with energy of the order of $100kT/q$ ($=1/2m\mu^2E^2$). Increase in lattice temperature, increases carrier energy only by few kT/q, which is far below the kinetic energy of accelerating electrons. Consequently, lattice temperature can play a role in increasing carrier energy only at a cold electrode.

The other question which arises is why the rate at which current increases with time (slope, Fig. 3) increases with pulse voltage? This can be explained as following: as the pulse voltage increases, power dissipation at the hot electrode, due to electron–phonon scattering increases. This leads to faster change in phonon population at the hot electrode–CNT interface, which in-turn increases the phonon population at the cold electrode at a faster rate. This eventually leads to an increased rate of change in current with respect to time at higher pulse voltages. The mechanism discussed above only explains the rise in current with respect to time and dependence on pulse voltage; however the observations related to the nature of quasi-static characteristics are yet to be explored. Although tunneling through non-crossing sub-bands[29,32] (Fig. 8a) can be safely considered to be responsible for the exponential increase in current with pulse voltage; however, it does not explain why the exponent increases for longer pulses. This behavior, together with the exponential increase in current with pulse voltage, indicates involvement of field as well as temperature dependent parameters.

Fig. 8 depicts tunneling of minority carriers through crossing and non-crossing sub-bands and the Fermi–Dirac distribution. In the case of direct or remote joule heating of the channel, the Fermi–Dirac distribution smears out to higher emerging. This, in case of electrons, populates energy states above the valance band edge or excites electrons from low energy non-crossing sub-bands to higher energy crossing sub-bands. It can also be seen as an increase in energy of a fraction of electrons present in the valance sub-bands, which lowers the tunneling distance for electrons to tunnel from the valance band to the conduction band, and improves the tunneling current. As discussed earlier, as the temperature across the MWCNT increases with pulse duration, the physical mechanism discussed above explains why tunneling current increases with pulse duration. The remote joule heating enhanced band-to-band tunneling is expected to take place simultaneously for holes, which increases the hole tunneling current with pulse duration, and contributes to the total current.

As explained earlier, remote joule heating can get accelerated at higher pulse voltages (temperature $\propto$ dissipated power $= V^2/R$), which in turn can also cause an exponential increase in current with pulse voltages, assuming the current is not limited by the number of modes present for conduction. However, in case of few shell CNTs or CNTs with smaller diameters, carrier transport assisted by remote joule heating would be limited by number of conduction modes available. Hence accelerated remote joule heating at higher fields should only be a cause for exponential increase in current for thicker CNTs.

So far we have found (i) field enhanced remote joule heating and (ii) remote joule heating enhanced tunneling through non-crossing sub-bands to be responsible for an exponential increase

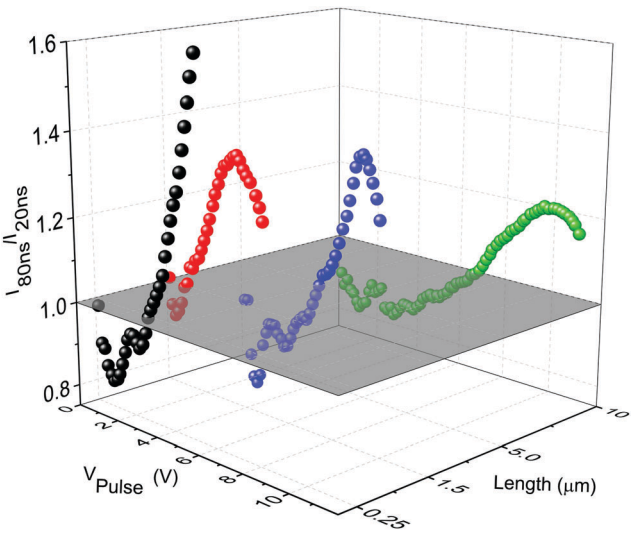

Fig. 9 Ratio of current measured at 80 and 20 ns with respect to pulse voltage for different CNT lengths.

in current with pulse voltage and higher exponents for longer duration pulses. To quantify this further, length dependence of remote joule heating carrier transport and band-to-band tunneling is studied in Fig. 9, which shows the ratio of current measured at 80 and 20 ns *vs.* pulse voltage for MWCNTs with different lengths. In principle, based on the discussion presented above, the ratio should be greater than 1 in the presence of remote joule heating assisted carrier transport and BTBT. For shorter tubes, with length sufficiently below the thermal diffusion length ($=\sqrt{D \times t}$, where D is thermal diffusivity and t is pulse time) this ratio is always expected to be higher than 1. The remote joule heating assisted band-to-band tunneling will always be present, however it will be triggered at higher pulse voltages as the CNT length increases. However, for longer tubes, with length greater than or close to the thermal diffusion length remote joule heating assisted carrier transport will get diminished. This will result in the overall ratio to fall and stay below that measured for shorter tubes. These predictions can be well observed in Fig. 9. Finally, a negative slope in the ratio *vs.* pulse voltage characteristics can also be noticed for longer tubes and at higher voltages. The drop in the ratio of currents is due to the current measured at 80 ns being lower than that measured at 20 ns for a given pulse voltage. This behavior is attributed to the diffusive nature of carrier transport in the case of longer tubes (length greater than mean scattering length). The diffusive transport current falls at a much faster rate as electron–phonon scattering increases. Moreover, the device configuration under test results in collapse of longer tubes on the SiO_2 surface, which not only results in enhanced boundary scattering but also removes the excess heat from the tube.[33,34] Attributed to enhanced electron–phonon scattering and boundary scattering, the current falls with respect to time for longer tubes,[35] which results in a lower current at 80 ns compared to that measured at 20 ns. On the other hand, heat removal by the substrate avoids remote joule heating assisted carrier transport. These mechanisms together mitigate increase in current with respect to time for longer tubes.

4 Conclusion

In summary, electrical transport through MWCNTs was explored at nanosecond time scales. The precise measurement technique revealed the remote joule heating assisted carrier transport and band-to-band tunneling. This role of remote joule heating was found to be more significant in ballistic and suspended tubes compared to diffusive and collapsed tubes. The precise and controllable nature of the technique proposed makes it a powerful tool to investigate mesoscopic effects, which often becomes difficult to probe using conventional techniques due to coupling between electrical and thermal transport.

Acknowledgements

The authors thank Prof. Srinivasan Raghavan (CeNSE, IISc), Prof. K. K. Nanda (MRC, IISc), Mr Ravi Nandan (MRC, IISc), Dr T. V. Prabhakar (DESE, IISc) for their help in material synthesis and setting-up the measurement system. A. M. thanks Mr Adil Meersha and Mr Yasasvi for their suggestions on device fabrication process. The work was financially supported by Department of Science and Technology, Government of India (project grant number: SB/S3/EECE/063/2014).

References

1 S. Iijima, *Nature*, 1991, **354**, 56–58.
2 H. J. Li, W. G. Lu, J. J. Li, X. D. Bai and C. Z. Gu, *Phys. Rev. Lett.*, 2005, **95**, 086601.
3 B. Wei, R. Vajtai and P. Ajayan, *Appl. Phys. Lett.*, 2001, **79**, 1172–1174.
4 S. Frank, P. Poncharal, Z. L. Wang and W. A. de Heer, *Science*, 1998, **280**, 1744–1746.
5 Z. Yao, C. L. Kane and C. Dekker, *Phys. Rev. Lett.*, 2000, **84**, 2941.
6 J.-Y. Park, S. Rosenblatt, Y. Yaish, V. Sazonova, H. Üstünel, S. Braig, T. A. Arias, P. W. Brouwer and P. L. McEuen, *Nano Lett.*, 2004, **4**, 517–520.
7 E. Pop, S. Sinha and K. E. Goodson, *Proc. IEEE*, 2006, **94**, 1587–1601.
8 P. G. Collins, M. Hersam, M. Arnold, R. Martel and P. Avouris, *Phys. Rev. Lett.*, 2001, **86**, 3128–3131.
9 J. Y. Huang, S. Chen, S. H. Jo, Z. Wang, D. X. Han, G. Chen, M. S. Dresselhaus and Z. F. Ren, *Phys. Rev. Lett.*, 2005, **94**, 236802.
10 M. Shrivastava, N. Kulshrestha and H. Gossner, *IEEE Trans. Device Mater. Reliab.*, 2014, **14**, 555–563.
11 N. Hamada, S.-i. Sawada and A. Oshiyama, *Phys. Rev. Lett.*, 1992, **68**, 1579.
12 P. Avouris, Z. Chen and V. Perebeinos, *Nat. Nanotechnol.*, 2007, **2**, 605–615.
13 L. Lu, W. Yi and D. Zhang, *Rev. Sci. Instrum.*, 2001, **72**, 2996–3003.
14 W. Yi, L. Lu, Z. Dian-Lin, Z. Pan and S. Xie, *Phys. Rev. B: Condens. Matter Mater. Phys.*, 1999, **59**, R9015.

15 D. J. Yang, Q. Zhang, G. Chen, S. F. Yoon, J. Ahn, S. G. Wang, Q. Zhou, Q. Wang and J. Q. Li, *Phys. Rev. B: Condens. Matter Mater. Phys.*, 2002, **66**, 165440.
16 F. Bussolotti, L. D'Ortenzi, V. Grossi, L. Lozzi, S. Santucci and M. Passacantando, *Phys. Rev. B: Condens. Matter Mater. Phys.*, 2007, **76**, 125415.
17 A. Bachtold, M. S. Fuhrer, S. Plyasunov, M. Forero, E. H. Anderson, A. Zettl and P. L. McEuen, *Phys. Rev. Lett.*, 2000, **84**, 6082–6085.
18 A. Stetter, J. Vancea and C. H. Back, *Phys. Rev. B: Condens. Matter Mater. Phys.*, 2010, **82**, 115451.
19 Y. Otsuka, Y. Naitoh, T. Matsumoto and T. Kawai, *Appl. Phys. Lett.*, 2003, **82**, 1944–1946.
20 J. Lee, A. Liao, E. Pop and W. P. King, *Nano Lett.*, 2009, **9**, 1356–1361.
21 J. Moscatello, V. Kayastha, B. Ulmen, A. Pandey, S. Wu, A. Singh and Y. K. Yap, *Carbon*, 2010, **48**, 3559–3569.
22 Kevin D. Ausman, R. Piner, O. Lourie, R. S. Ruoff and M. Korobov, *J. Phys. Chem. B*, 2000, **104**, 8911–8915.
23 M. Tsutsui, Y.-k. Taninouchi, S. Kurokawa and A. Sakai, *J. Appl. Phys.*, 2006, **100**, 094302.
24 H.-Y. Chiu, V. Deshpande, H. C. Postma, C. Lau, C. Miko, L. Forro and M. Bockrath, *Phys. Rev. Lett.*, 2005, **95**, 226101.
25 S. Datta, *Electronic Transport in Mesoscopic Systems*, Cambridge University Press, 1997.
26 S. Kaur, N. Raravikar, B. A. Helms, R. Prasher and D. F. Ogletree, *Nat. Commun.*, 2014, **5**, 3082.
27 P. M. F. J. Costa, U. K. Gautam, Y. Bando and D. Golberg, *Nat. Commun.*, 2011, **2**, 421.
28 K. Schwab, E. A. Henriksen, J. M. Worlock and M. L. Roukes, *Nature*, 2000, **404**, 974–977.
29 M. P. Anantram, *Phys. Rev. B: Condens. Matter Mater. Phys.*, 2000, **62**, R4837–R4840.
30 A. Naeemi and J. D. Meindl, *IEEE Electron Device Lett.*, 2006, **27**, 338–340.
31 J. H. Lienhard, *A heat transfer textbook*, Phlogiston Press, 2013.
32 A. Svizhenko, M. P. Anantram and T. R. Govindan, *IEEE Trans. Nanotechnol.*, 2005, **4**, 557–562.
33 K. H. Baloch, N. Voskanian, M. Bronsgeest and J. Cumings, *Nat. Nanotechnol.*, 2012, **7**, 316–319.
34 S. V. Rotkin, V. Perebeinos, A. G. Petrov and P. Avouris, *Nano Lett.*, 2009, **9**, 1850–1855.
35 B. Bourlon, D. Glattli, B. Plaçais, J.-M. Berroir, C. Miko, L. Forro and A. Bachtold, *Phys. Rev. Lett.*, 2004, **92**, 026804.

